Available online at www.sciencedirect.com

jmr&t Journal of Materials Research and Technology

journal homepage: www.elsevier.com/locate/jmrt

Original Article

Investigation on polypropylene friction stir joint: effects of tool tilt angle on heat flux, material flow and defect formation

Guangle Fan [a], *Jacek Tomków* [b,*], *Mahmoud E. Abdullah* [c], *Hamed Aghajani Derazkola* [d,**]

[a] *Department of Materials Science and Engineering, Texas A&M University, 575 Ross Street, College Station, TX, 77843, USA*

[b] *Institute of Manufacturing and Materials Technology, Faculty of Mechanical Engineering and Ship Technology, Gdańsk University of Technology, Gabriela Narutowicza Street 11/12, 80-233, Gdańsk, Poland*

[c] *Mechanical Department, Faculty of Technology and Education, Beni-Suef University, Beni-Suef, 62511, Egypt*

[d] *Department of Mechanics, Design and Industrial Management, University of Deusto, Avda Universidades 24, 48007, Bilbao, Spain*

ARTICLE INFO

Article history:
Received 27 October 2022
Accepted 4 January 2023
Available online 13 January 2023

Keywords:
Tool tilt angle
Friction stir joining
Computational fluid dynamic
Polypropylene

ABSTRACT

Tool tilt angle (TTA) is a critical factor that can control material flow in polymeric materials' friction stir joining (FSJ). This study selected a TTA range between 0° to 4° for FSJ of polypropylene (PP) polymer sheet. A modified computational fluid dynamic (CFD) technique was implemented to gain a deep understanding of the effects of TTA during FSJ of PP. The PP joint's internal flow, defect formation, heat generation, and tensile strength were investigated experimentally. The fracture surface of tensile samples was analyzed by scanning electron microscopy (SEM). Heat generation, heat flux, and defect formation results from simulation were evaluated by experimental tests output. The results indicate that the PP flow during FSJ is susceptible to TTA. Non-uniform volumetric weight transfer was caused at higher TTA in the joint line, which leads to tilted heat flux. At higher TTA, the generated heat increases, leading to PP exit from the joint line and internal gaps. According to selected parameters, the most robust joint (66 MPa) was produced at 1° TTA. The main reason for the mechanical properties of the PP joint was a dimension of the stir zone and internal defects. Shrinkage gaps were the root of crack initiation during the tensile test, and some local stretching in the fracture surface of the tensile sample after the test was detected.

* Corresponding author.
** Corresponding author.
E-mail addresses: jacek.tomkow@pg.edu.pl (J. Tomków), h.aghajani@deusto.es (H.A. Derazkola).

https://doi.org/10.1016/j.jmrt.2023.01.028

1. Introduction

Polymers and polymeric matrix composites are widely employed in many applications in the automobile and railway industries. Lower cost, more processability, recyclability, and flexible maintenance caused the high application of polymeric materials in various industries [1]. In addition, thermoplastics with high strength-to-weight ratios are increasingly involved in structural applications [2]. The selection of a suitable welding process for polymers is a key factor in the manufacturing of reliable structures. Conventional joining techniques for polymers like adhesive bonding, mechanical fastening, infrared radiation (IR), and even thermal welding processes show various disadvantages and limitations [3]. To this end, advanced welding techniques such as laser welding, laser-assisted joining, and friction stir joining (FSJ) provide significant advantages and decrease joint defects after welding polymeric materials [4]. In the early stages, the FSJ was first applied to join Al alloys [5]. After discovering various benefits of this joining process, FSJ has been used to join various similar and dissimilar materials, including metals, thermoplastics, and composites [6]. The required heat for welding during the FSJ process is provided by friction at contact surfaces between a non-consumable tool and workpieces [7]. The tool with rotational velocity increased the temperature of the joint line below that of melting point and mixed workpieces together [8]. There is no external filler material or external heat source during the FSJ process, similar to the linear friction welding process [9,10].

For this reason, FSJ is called a solid-state joining process, and the structure of the joint line has minimal changes compared to other joining methods [11]. These properties decrease the possible formation of internal defects in the joint line [12]. Low heat input and flexibility make the FSJ process a suitable welding technique for polymeric materials [13]. FSJ tool rotational velocity, traverse velocity, tilt angle, and plunge depth are the main process parameters in this welding process [14]. Due to the highly sensitive polymeric material, selecting suitable process parameters is very important. FSJ has been applied to the welding of polymers and thermoplastic materials [15].

Azarsa and Mostafapour [16] optimized the tool rotational and traversed velocity of the FSJ tool while welding of high density polyethylene (HDPE) sheets. They indicated that by controlling FSJ tool velocities, the heat input in the joint line would be controlled, and the ultimate tensile strength of the final joint can be reached near welds 75% of HDPE. It is shown that a tool with a threaded pin can reduce cavities and inclusions in the joint line after the FSJ process of polypropylene (PP) sheets, and also it can improve the mechanical properties of the final joint. Panneerselvam and Lenin [17] show that during FSJ of polyamide 6 the rotation direction of the tool can change the mechanical properties of the final joint. They stated that the clockwise rotation direction of the FSJ tool could improve internal flow and the mechanical properties of the final joint [18].

Researchers developed the FSJ process by using a stationary shoulder called a "shoe" to improve the surface quality of polyethylene (PE) joints [19]. Also, it was possible to use an external heating system inside the ˙Shoë to increase the mechanical properties of the final joint as much as possible. This technique was implemented to joining of acrylonitrile butadiene styrene (ABS) sheets [20].

Simões and Rodrigues [21] studied Poly-methyl-methacrylate (PMMA) behavior during the FSJ process with various tool rotational and traverse velocities.

Among various process parameters during the FSJ process, the tool tilt angle (TTA) plays a critical role in producing sound joints [22]. The controlling tool tilt angle can significantly improve final mechanical properties [23]. The exit of materials from the joint line, surface flash formation, and joint root defects are the primary defects produced by the unappropriated tool tilt angle during FSJ of polymeric materials [24]. Limited literature focuses on the effects of FSJ tool tilt angle on the properties of polymeric materials joints. Aghajani Derazkola and Simchi [25] investigated the effects of FSJ tool tilt angle on the mechanical properties of PMMA sheets. They stated that the materials flow during FSJ is very sensitive to TTA, and for the appropriate TTA selecting of appropriate tool plunge depth is necessary. Eyvazian et al. [26] indicated that for the production of the highest strength joint during FSJ of PMMA joint, 2° TTA is needed. The joint root defects and weak mixing between raw sheets are the main defects that are produced at very high or very low TTA. Aghajani Derazkola et al. [24] showed that at high TTA, the surface flashes intensely formed during FSJ of the polycarbonate (PC) sheet. The surface flash decreases the joint line area, and consequently, the mechanical properties of the final joint decrease dramatically. TTA has been primarily considered in metallic materials joints and could be implemented differently. Zhai et al. [27] presented a new approach for the effects of TTA during FSJ of AA6061-T6 alloy. Their research considers two types of joints, one without tilt and another with a tilt angle. In the tilted case, they stated two types of contact. They considered a pin, a part of the shoulder was inside the workpiece, and the front of the shoulder that was not in touch with the workpiece. They implemented this assumption in real situations and modified the tool shoulder's velocity and contact surface during the simulation [28].

Among various polymeric materials, polypropylene (PP) has good mechanical and functional properties that caused this polymer to be considered by various industries [29]. Limited research focused on the FSJ of PP. Bilici [30] studied the effects of tool pin profiles on the properties of PP during the friction stir spot joining (FSSJ) process. The tool shoulder diameter, pin angle, and pin length were selected as the variable. Finally, the optimum tool geometry was found to achieve the highest tensile strength. Kiss and Czigány [31] studied on effects of tool rotational velocity on the morphology of the PP joint during the FSJ process. They stated that after FSJ, the complex supramolecular structure formed at the borderline of the joint, and the structure of the middle part of the joint line is similar to PP. Moochani et al. [32] used a new tool that contains an external heater for FSJ of PP. The tool was able to put controllable hot air on the joint line. They show that with this new mechanism during the FSJ process, the final joint's tensile strength reaches 99% of the base material. Sahu et al. [33] used artificial intelligence to optimum tool rotational velocity, tool traveling velocity, tool pin profile, and applied load during FSJ of PP. They show that optimizing process parameters can reach the joint tensile strength to the highest point.

Due to their result, a pin profile with a square shape was the best pin for the FSJ of PP. Nath et al. [34] studied the joining of PP by single-side and double-side FSJ. They show that the double-side FSJ process yields better mechanical properties of the final joint comparing single-side FSJ. They also implemented a self-heating tool for FSJ of PP [35]. This tool mechanism contained an extra nozzle for pouring hot air on the joint line. They show that the defect-free joint can be made with this tooling system, and internal materials flow improves significantly. Due to the wide application of PP, using the FSJ process for this polymer is necessary. For this reason, the effects of TTA on FSJ of PP in this study were assessed. For a better understanding of material flow and joining mechanism, a thermo-mechanical simulation process has been used in order to analysis of thermal history.

2. Modelling details

2.1. Assumptions

Technical point of view, the FSJ process has three different stages. The first stage is when the welding machine starts until the penetration of workpieces. In the second stage, the main stage of welding, the rotational FSJ tool starts to move forward and forms the joint line. The last stage is when the welding procedure is finished, and the rotational FSJ tool exits the joint line. For simplicity and to decrease the simulation time, the first and last stages of the FSJ process are ignored. During the moving of stage two, the FSJ tool had constant forward. For this reason, a steady-state coupled material flow and heat model was implemented to simulate the process. The CFD method was employed to analyze thermo-mechanical phenomena during FSJ. A model was set up with exact dimensions for the workpiece and tool used during the experimental procedure to understand process parameter effects better. All parameters implemented with same dimension unites. The conservation equations for momentum, energy, and continuity were solved to analyze polymer flow during the joining process. The mass conservation is presented by Eq. (1), and momentum conservation in x, y, and z directions is presented by Eq. (2), and energy conservation is presented by Eq. (3) [36]:

$$\frac{\partial m_i}{\partial x_i}=0; \quad i=1,2,3 \tag{1}$$

$$\frac{\rho_c}{v}\frac{\partial m_j}{\partial t}+m_i\frac{\partial m_j}{\partial x_i}=-\frac{\rho_c}{v}\left[\frac{\partial P}{\partial x_j}+M\frac{\partial m_j}{\partial x_j}\right]+\frac{\partial}{\partial x_j}\left(\frac{\partial \varphi m_j}{\partial x_i}\right) \tag{2}$$

$$\frac{\rho_c}{v}\left[\frac{\partial (C_pT)}{\partial t}+\frac{\partial (C_pm_iT)}{\partial x_i}\right]=-\frac{\rho_c}{v}C_pM\frac{\partial T}{\partial x_1}+\frac{\partial}{\partial x_i}\left(k\frac{\partial T}{\partial x_i}\right)+D_{Total} \tag{3}$$

In Eqs. (1)–(3), the m_i is representing the flow of material in the x, y, and z direction and P is pressure. P is the relative pressure that drives flow in the x, y, and z directions [37]. The ρ_c, C_p, v and k are density, specific heat, pressure depend volume of PP (with cubic meter unit), and thermal conductivity of polymer base metal depending on temperature. The $\frac{\rho_c}{v}$ is defined as pressure-volumetric depend density with kg/m^3 unit. The used specific heat and thermal conductivity of PP in this study at various temperatures are depicted in Fig. 1a and b, respectively. The date in Fig. 1 obtained from testing raw PP in laboratory. In Eq. (5), the term D_{Total} represents the total heat input produced by friction and plastic deformation.

2.2. Thermal model

In section 3.1. The term D_{Total} in Eq. (3) was introduced as a heat source [36]. During the FSJ process, the internal heat source is the sum of frictional heat and plastic deformation of base material that generates during the forward moving of the rotational tool [38]. The frictional heat presented by $D_{friction}$ and heat generated by plastic deformation heat is presented by $D_{plastic}$. In this case, the D_{Total} is defined as [38]:

$$D_{Total}=D_{friction}+D_{plastic} \tag{4}$$

The generated heat by friction ($D_{friction}$) consists of generation heat at interface of shoulder-workpiece (D_{sw}), pin body-workpiece (D_{bw}), and pin beneath-workpiece (D_{tw}) [39]:

$$D_{friction}=D_{sw}+D_{bw}+D_{tw} \tag{5}$$

The D_{sw}, D_{bw}, and D_{tw} for 0° tilt angle are defined by [40]:

$$D_{sw}=\int_0^{2\pi}\int_{R_b}^{R_s} h_w\left[\eta(1-\delta)\varphi+\delta\mu_f F_z\right]\times\left(\frac{2\pi\omega r^2-Mr\sin\theta}{60}\right)drd\theta \tag{6}$$

$$D_{bw}=\int_0^{2\pi}\int_{R_b}^{R_b} h_w\varphi\left[\eta(1-\delta)+\sqrt{3}\,\delta\mu_f\right]\times\left(\frac{2\pi\omega r-M\sin\theta}{60}\right)r(z)dzd\theta \tag{7}$$

$$D_{tw}=\int_0^{2\pi}\int_{R_p}^{R_p} h_w\left[\eta(1-\delta)\varphi+\delta\mu_f F_z\right]\times\left(\frac{2\pi\omega r^2-Mr\sin\theta}{60}\right)drd\theta \tag{8}$$

The R_s, R_p and R_b present the tool shoulder radius, pin body radius, and pin beneath radius, respectively. The h_w is conducted heat into the weld material, η is plastic deformation efficacy (0.5 selected in this study), δ is fractional slip (0.4 selected in this study), φ is polymer flow stress that will define in next section. In Eqs. (8)–(10), the μ_f is friction coefficient (0.4 selected in this study), M is the welding velocity, F is axial force (50 N selected in this study), and ω is shown rotational velocity of the FSJ tool. From the process point of view, the axial force is the amount of force transferred by the FSJ machine on the tool and stir zone. The axial force in 0° tilt case is equal to F_z. In the tilted case, the tool force is not applied to the workpiece's according to the workpiece normal vector. A schematic view of forces and loads on the tool is depicted in Fig. 2. The axial force (F) is divided into two normal (F_z) and shear (F_x) forces. The values for Fz and Fx are cosines and sines of tilted angle multiple with axial force. In the tilted case, the reference point (RP) is considered to insert all parts of tool inside the workpiece. There is not any non-contact surface in the tilted case of this study. Plus, at this point, when the RP touches the top surface of PP, a part of tool body inserts into the PP that called excess area (EA). In such case, the EA is produced an amount of frictional heat (D_{EA}) that is very close to tool pin body frictional heat generation.

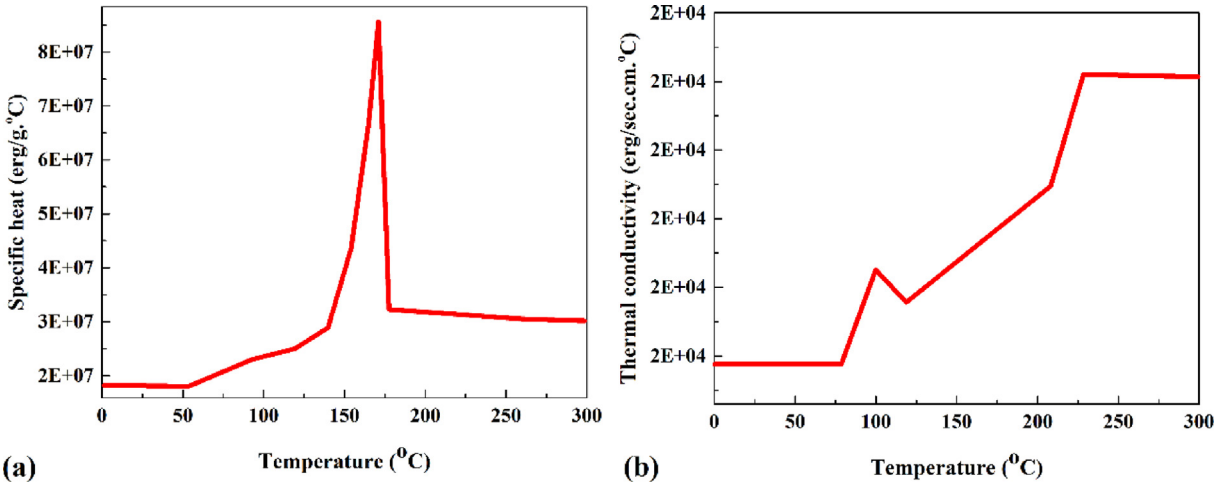

Fig. 1 – (a) Specific heat and (b) thermal conductivity of PP.

Accordingly, the D_{sw}, D_{bw} and D_{tw} for tilted sample with the tilt angle (ξ) are defined by:

$$\int_0^{2\pi}\int_{R_b}^{R_s} h_w\left[\eta(1-\delta)\varphi+\delta\mu_f F_z\sqrt{\sin\zeta+\cos\zeta}\right]\times\left(\frac{2\pi\omega r^2-Mr\sin\theta}{60}\right)drd\theta \quad Normal\ Force$$

$$D_{sw}=\begin{cases}\int_0^{2\pi}\int_{R_b}^{R_s} h_w\left[\eta(1-\delta)\varphi+\delta\mu_f F_x\sqrt{\sin\zeta+\cos\zeta}\right]\times\left(\frac{2\pi\omega r^2-Mr\sin\theta}{60}\right)drd\theta & Shear\ Force\end{cases} \tag{9}$$

$$D_{bw}=\int_0^{2\pi}\int_{R_b}^{R_b} h_w\varphi\left[\eta(1-\delta)+\sqrt{3}\,\delta\mu_f\right]\times\left(\frac{2\pi\omega r-R\sin\theta}{60}\right)r(z)dzd\theta \tag{10}$$

$$\int_0^{2\pi}\int_{R_p}^{R_p} h_w\left[\eta(1-\delta)\varphi+\delta\mu_f F_z\sqrt{\sin\zeta+\cos\zeta}\right]\times\left(\frac{2\pi\omega r^2-Mr\sin\theta}{60}\right)drd\theta \quad Normal\ Force$$

$$D_{tw}=\begin{cases}\int_0^{2\pi}\int_{R_p}^{R_p} h_w\left[\eta(1-\delta)\varphi+\delta\mu_f F_x\sqrt{\sin\zeta+\cos\zeta}\right]\times\left(\frac{2\pi\omega r^2-Mr\sin\theta}{60}\right)drd\theta & Shear\ Force\end{cases} \tag{11}$$

$$D_{EA}=\int_0^{2\pi}\int_0^{R_s} h_w\varphi\left[\eta(1-\delta)+\sqrt{3}\,\delta\mu_f\right]\times\left(\frac{2\pi\omega r-R\sin\theta}{60}\right)r(z)dzd\theta \tag{12}$$

The amount of heat produced by plastic deformation can be defined by the following [41]:

$$H_p=\Psi\varphi\left[2\left(\left(\frac{\partial m_1}{\partial x_1}\right)^2+\left(\frac{\partial m_2}{\partial x_2}\right)^2+\left(\frac{\partial m_3}{\partial x_3}\right)^2\right)+\left(\frac{\partial m_2}{\partial x_1}+\frac{\partial m_1}{\partial x_2}\right)^2+\left(\frac{\partial m_1}{\partial x_3}+\frac{\partial m_3}{\partial x_1}\right)^2+\left(\frac{\partial m_3}{\partial x_2}+\frac{\partial m_2}{\partial x_3}\right)^2\right] \tag{13}$$

in Eq. (13), ψ is a constant that specifies the internal mixing of polymer in the stir zone.

2.3. *Material model*

During simulation of the process, the density of the used polymer was defined by pressure depend volume ($\frac{\rho_c}{v}$). This term is used in Eq. (3) and detailed there. The specific volume (v) of the PP is a comparable property that depends on applied pressure and temperature during processing of polymeric materials. The specific volume is defined by a pressure-volume-temperature (P-V-T) diagram. This material model was used in this study because the pressure and temperature in stir zone are local. For this reason, the specific volume of PP in stir zone changes during the heating up, stirring action, and cooling of joint line. The P-V-T diagram for the PP that used in this study is presented in Fig. 3.

The polymer viscosity as a function of flow stress and effective strain rate can be defined by [42]:

$$\varphi=\varepsilon_{ij}\exp\left(-\frac{\Delta U}{R\overline{T}}\right)\sinh\left(\frac{\sigma_e V^*}{B\overline{T}}\right) \tag{14}$$

In Eq. (14), the ε_{ij}, ΔU, V^*, and R, are activation strain, activation energy, activation volume, and gas constant, respectively. The $\overline{T}$, presented as [42]:

$$\overline{T}=T+\left(T_{g,dry}-T_{g,wet}\right) \tag{15}$$

In this equation the T is actual temperature. $T_{g,dry}$ and $T_{g,wet}$ are the glass transition temperature at the dry state and glass transition temperature after FSJ. The $T_{g,dry}$ and $T_{g,wet}$ achieved by differential scanning calorimetry (DSC) test before and

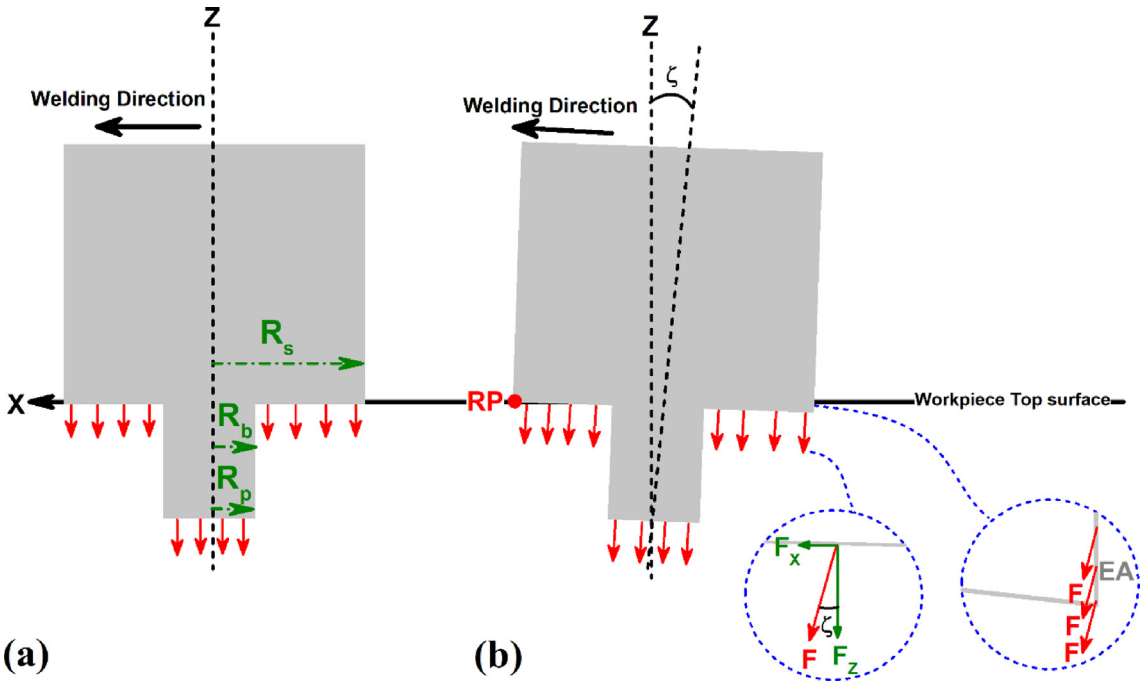

Fig. 2 – Schematic view of an applied force by FSJ tool.

after FSJ process. As mentioned, the ε_{ij} is effective stain that defined by [42]:

$$\varepsilon_{ij} = \int_0^{t_f(\sigma,T)} \dot{\varepsilon}_{ij}(\sigma,T)dt_f(\sigma,T) \quad (16)$$

In Eq. (16), the $\dot{\varepsilon}_{ij}(\sigma,T)$ and $dt_f(\sigma,T)$ are presents the polymer flow rate as function of load and temperature and time-to-flow. Despite the metallic materials, the polymers should be warmed up until the softening temperature. At that temperature, they can be stirred by the tool. In this situation the time to start the softening presented as "time-to-flow".

2.4. *Void formation*

One of the central issues in FSJ of polymers is bubbles in SZ. It is approved that the bubbles are trapped air from the environment into SZ and shrinkage bubbles of polymeric materials after plasticization and re-solidification after FSJ. The shrinkage equations have been added to the CFD model for void formation analysis. The shrinkage of PP after passing the FSJ tool through SZ can be predicted by temperature-dependent pressure (P_t) after FSJ and polymer flow pressure at ambient temperature (P_0) [42]:

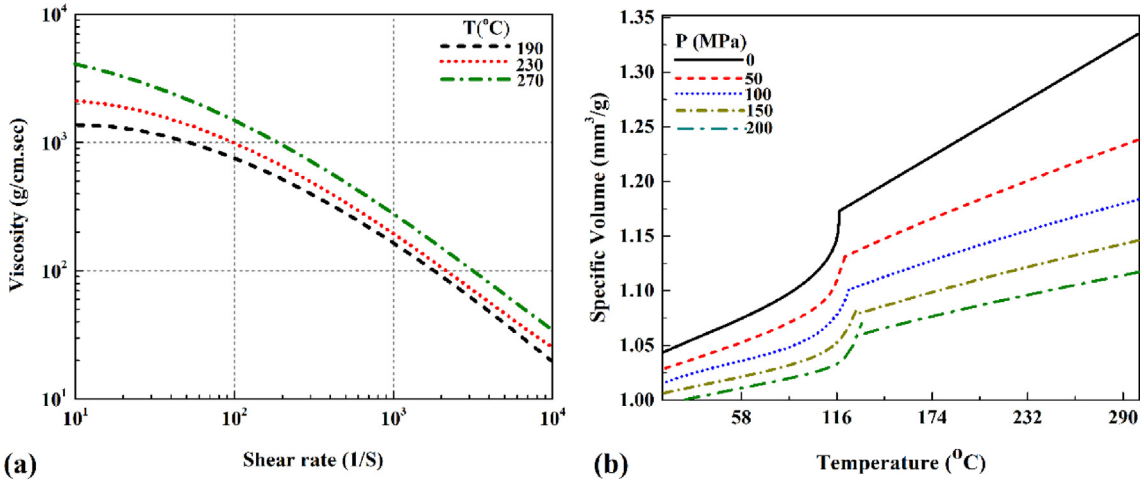

Fig. 3 – (a) Viscosity and (b) Specific volume of PP.

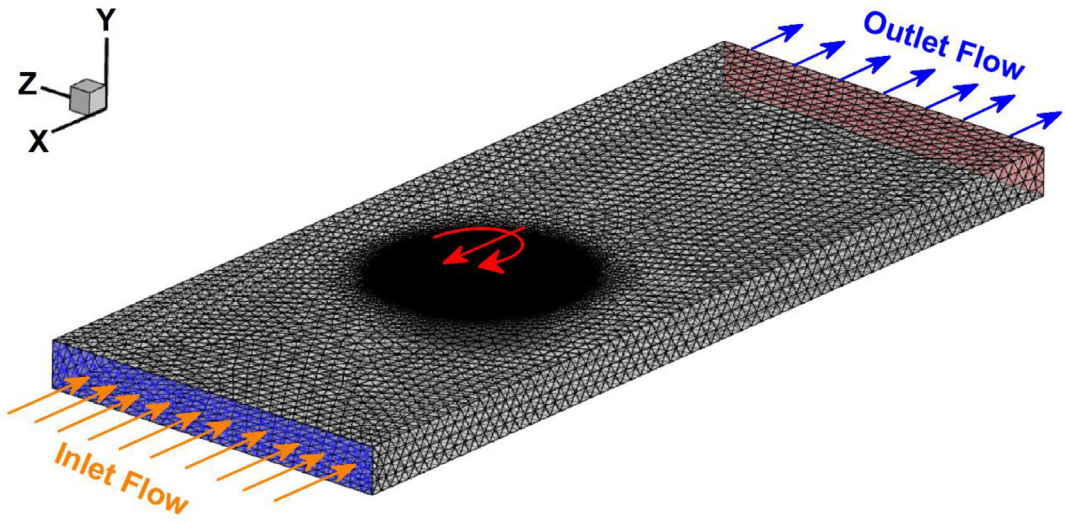

Fig. 4 – FSJ area after mesh.

$$Sh(t) = 1 - \frac{P(t)}{P_0} \tag{17}$$

2.5. *Heat transfer model*

In this study, the initial and ambient temperatures were selected at 300 K. The heat transfer models at different interfaces were selected. A part of PP that was in touch with the welding fixture had a conductive heat transfer model by [43]:

$$k\frac{\partial T}{\partial Z}\Big|_{Bottom} = h_b(T - T_a) \tag{18}$$

The heat transfer coefficient at the bottom face depended on the local temperature through the following Equation [44]:

$$h_b = h_{b0}(T - T_a)^{0.25} \tag{19}$$

At the sides and top surface, convective and radiation heat transfers were assumed [45]:

$$-k\frac{\partial T}{\partial Z}\Big|_{Top} = B \in (T^4 - T_a^4) + h_b(T - T_a) \tag{20}$$

The picture from meshed FSJ area is presented in Fig. 4.

3. Experimental tests

The PP sheets are provided from the local market and selected as weldments. The raw sheets have 4 mm thick and cut 60 × 100 mm for the welding procedure. A modified milling machine has done the FSJ. The FSJ tool had a frustum pin. The shoulder diameter, pin diameter, and pin length were 16 mm, 8 mm, and 3 mm, respectively. Fig. 5 is depicted the tool used in this study. A fixture was set up on the welding machine to position the raw sheets and fix them during the FSJ process. In

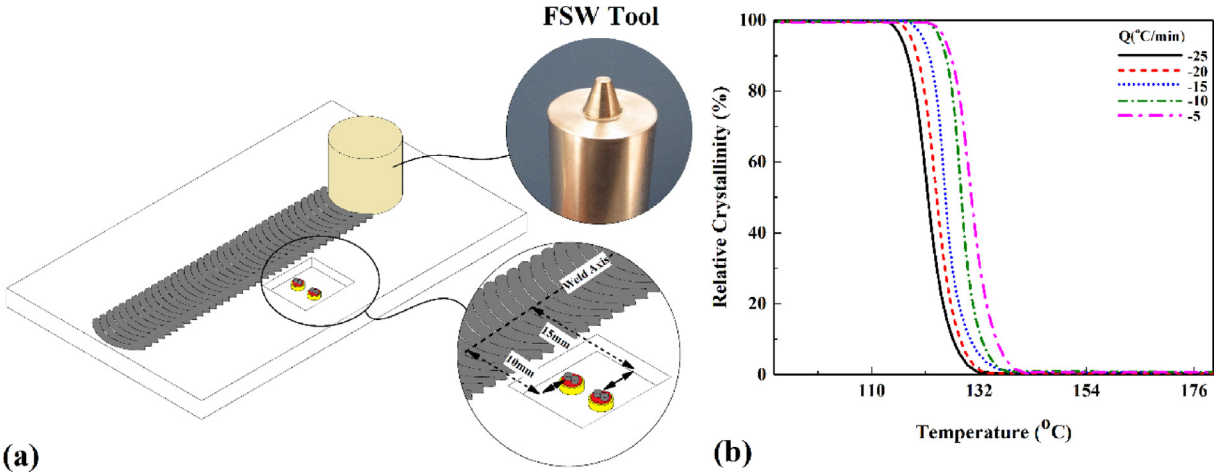

Fig. 5 – (a) Used FSJ tool and thermocouples places, (b) Crystallinity of PP.

Table 1 – FSJ process parameters.

sample	Tool rotation (rpm)	Welding velocity (mm/min)	Tool plunge depth (mm)	Tool tilt angle (degree)
0	730	20	0.15	0
1	730	20	0.15	1
2	730	20	0.15	2
3	730	20	0.15	3
4	730	20	0.15	4

these experiments, the tool had 930 rpm rotational and 30 mm/min traveling speeds and 0.15 mm plunge depth. During this study, the tool tilt angle was selected as the variable. Tool revolution pitch is defined to unify the tool speed during the process. The welding process parameters are listed in Table 1.

For the recording of thermal history during the FSJ process, the maximum heat in the joint line was recorded by thermocouples. For this reason, two thermocouples (J-type) were placed inside the polypropylene sheets. A schematic view for the thermocouple placements is presented in Fig. 5a. For better analysis of internal material flow on optical microscopy, carbon tape was put at the interface of PP interfaces. Internal and surface materials flow from welded samples was evaluated by optical microscopy. A tensile test was done on the welded samples according to ASTM D638 standard. After the test, the fracture surface of tensile samples was evaluated by scanning electron microscopy (SEM). The DSC analysis was done on the PP for analysis of the PP at various temperatures. The crystallinity of PP obtained from DSC is used in simulation results. The DSC analysis graphs are presented in Fig. 5b.

4. Results and discussions

4.1. *Heat generation*

This section investigates the analysis of simulation results about heat generation by each FSJ tool part. From an experimental point of view, analyzing heat generation by a different part of FSJ is very hard and, in some cases, impossible. For this reason, the simulation results give a good knowledge about the analysis of heat generation y different parts of the FSJ tool. The simulation results from maximum heat generation by FSJ tool shoulder, tool pin body, tool pin beneath, and EA is presented in Fig. 6a, b, 6c, and 6d, respectively. All results show that with increasing TTA, the generated heat at the interface of PP and tool parts increases. From generate heat section, it can be concluded that the tool shoulder generates the

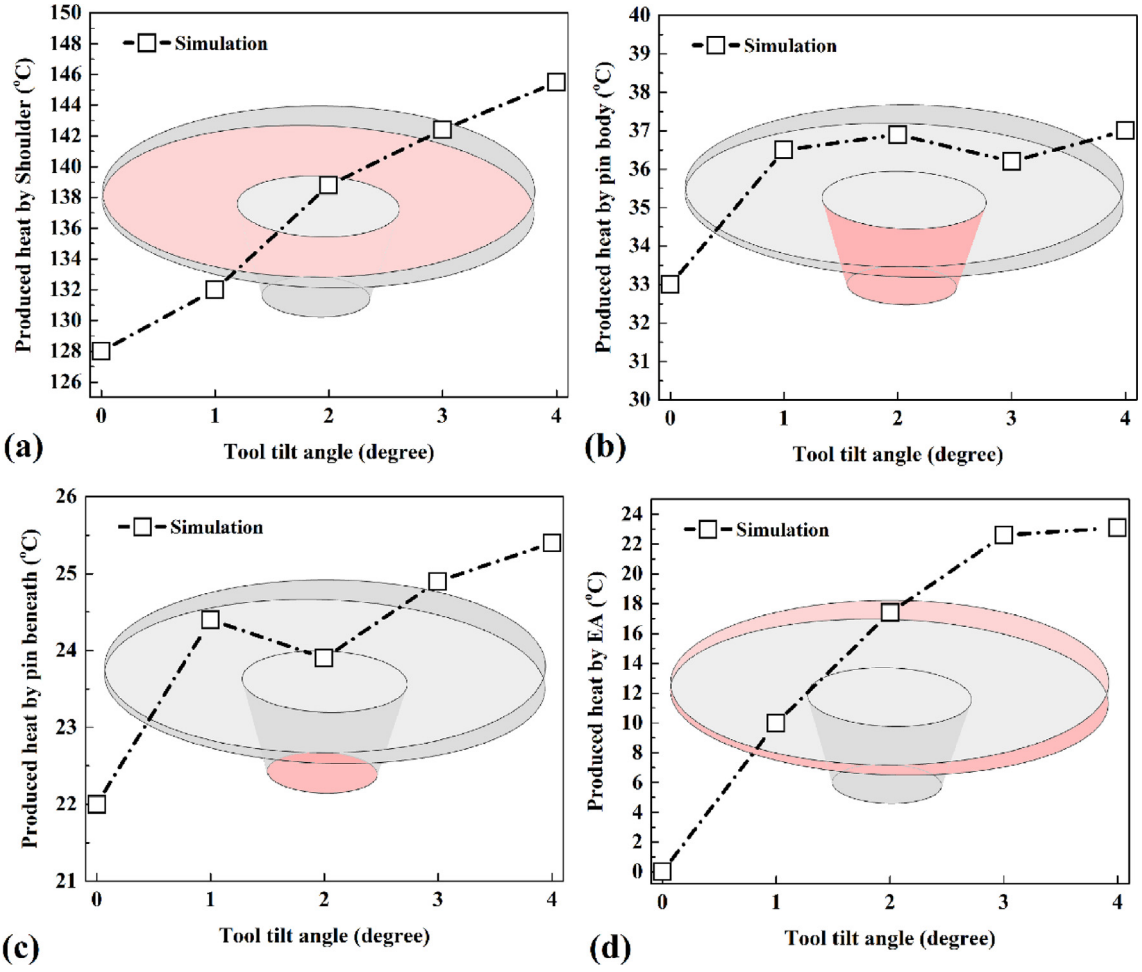

Fig. 6 – Simulation results of heat generation by (a) tool shoulder, (b) tool pin body, (c) tool pin beneath, and (d) EA.

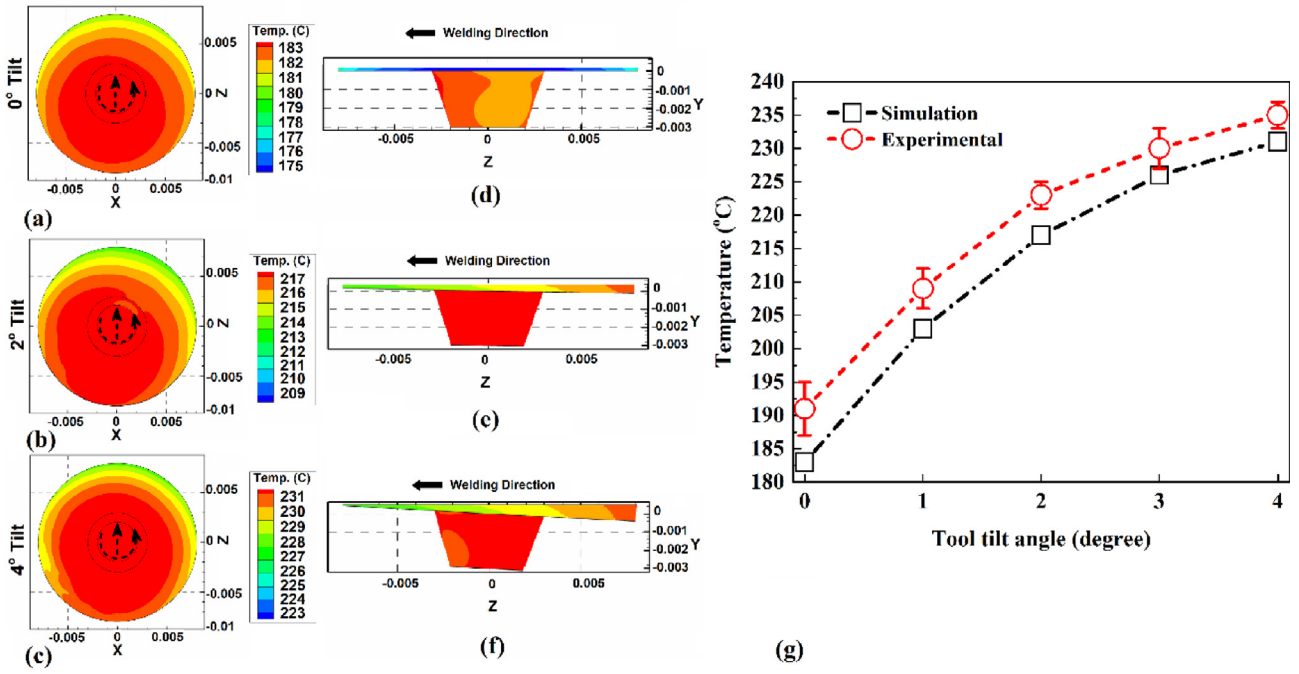

Fig. 7 – Top view of SZ from simulation result of joint that jointed by (a) 0°, (b) 2°, and (c) 4°. Side view of SZ from simulation result of joint that jointed by (d) 0°, (e) 2°, and (f) 4°, (g) Comparison between simulation results and maximum heat that recorded by thermocouples.

majority of the heat, and the minority of heat is generated in the EA area.

This trend is seen in all TTA. In the case of 0° tilt angle, EA does not produce any heat, so the majority of heat is produced by the tool shoulder. Because the normal force on the interface of the tool body and EA is meagre, the frictional heat generation in this area is minimal. Parallel contact between the tool body and EA indicates that heat generation in this area is related to the hook shear stress during the rotational movement of the tool. It means the plastic deformation heat in the EA area is more than frictional heat generation during FSJ. The results indicate that the heat generation by shoulder, pin body, pin beneath, and EA in 0° TTA is 70%, 20%, and 10% of total heat. The result indicates that the tool shoulder, pin body, pin beneath, and EA produced 64%, 16%, 12%, and 6% of total heat.

The simulation results of heat flow in the stir zone (SZ) give good information about the combination of generated heat made by a different part of the tool. The top view of SZ of cases that FSJed by 0°, 2°, and 4° TTA is presented in Fig. 7a, b, and 7c, respectively. Due to obtained results, the heat concentration in all samples was the backside of the shoulder and pin body. With increasing TTA, the hot area at the backside of SZ increases. In 0° TTA, the hot rings in SZ are almost concentric, with the highest temperature circle in the centre. With increasing TTA, the heat production leads to the formation of the eccentric hot circular regime inclined to the tool's rear edge. The side view of samples that FSJed by 0°, 2°, and 4° TTA is presented in Fig. 7d, e, and 7f, respectively. The results clearly approved that with increasing TTA, the heat concentration at the backside of the pin increases. The simulation results and maximum temperature recorded by thermocouples are presented in Fig. 7g. The maximum simulation results were lower than the experimental data. In general, the simulation results had good agreement with the experimental results. The simulation results indicate that the maximum temperature in the PP joint that FSJed by 0°, 1°, 2°, 3°, and 4° TTA, are 184 °C, 204 °C, 215 °C, 223 °C, and 231 °C. The maximum heat recorded during FSJ of PP with 0°, 1°, 2°, 3°, and 4° TTA, is 192 °C, 209 °C, 224 °C, 230 °C, and 235 °C, respectively.

Heat generation directly affects the formation, size, and dimension of SZ. The cross-section view of the FSJed sample with 2° TTA is presented in Fig. 8a for general analysis. The joint line consists of an SZ and a heat-affected zone (HAZ) formed in the vicinity of the SZ. The produced heat in SZ diffused into the surroundings and made the HAZ area. Due to the low heat transfer coefficient of PP, the HAZ in this joint was narrow. For better analysis of the relation between TTA heat and SZ dimensions, the SZ of the selected sample was manually measured (Fig. 8b). Then, the geometry of the experimental result was compared by the size of SZ that obtained by thermal results from the simulation (Fig. 8c). In this step the simulation results and experiments had a good agreement. The CFD simulation shows an increasing trend in generated heat at joints of more than 2°. In the real joints, high EA in TTA of more than 2o decreases the size of SZ. The experimental results show that at high TTA, the material exploded from the joint line, and the final size of SZ in 3° to 4° decreases. The high EA obstacle to extruding materials from the front of the tool to the SZ and the final size of SZ in these TTA decreases. High TTA forms defected SZ in joint line, and

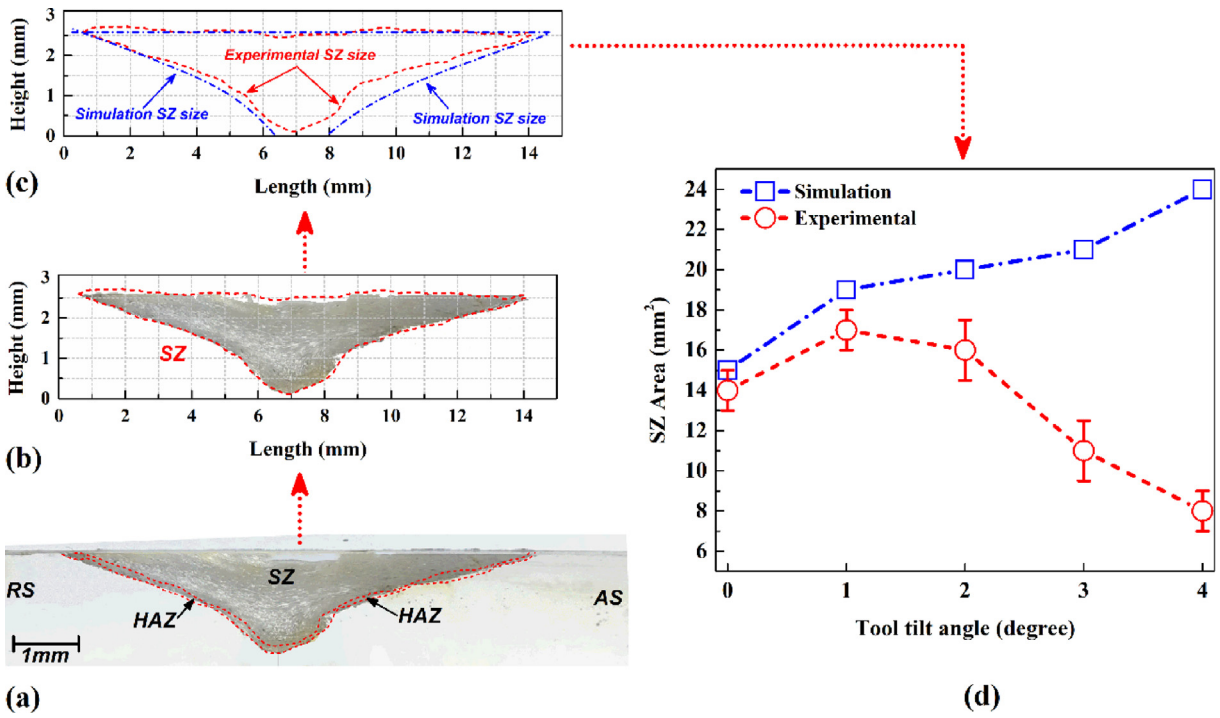

Fig. 8 – (a) Cross-section view of 2° TTA joint. (b) geometrical measurement from SZ area of 2° TTA joint. (c) comparison between real and simulation output dimension for 2° TTA joint. (d) comparison of FSJ joint SZ and simulation output for all cases.

material exit behaviour is impossible to simulate in fluid dynamic simulation. For this reason, the prediction of SZ by simulation is not matching with actual joints. The measured stir zone area in 0°, 1°, 2°, 3° and 4° TTA was 13 mm^2, 17 mm^2, 16 mm^2, 11 mm^2 and 8 mm^2, respectively.

4.2. *Heat flux and surface material flow*

The surface heat flow can show the surface heat flux of PP during thermo-mechanical phenomena. The surface heat flux is related to the chemical properties of PP, but the mechanical

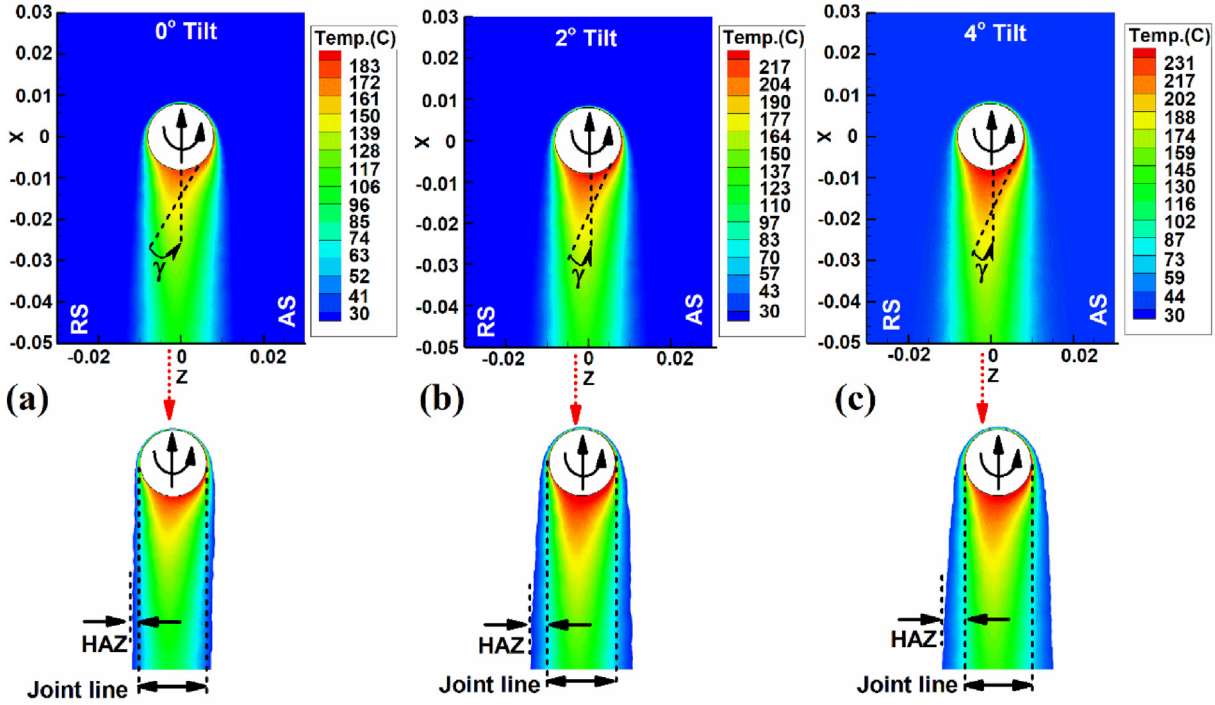

Fig. 9 – Simulation results of surface heat flux at joint that FSJed with (a) 0°, (b) 2°, and (c) 4° TTA.

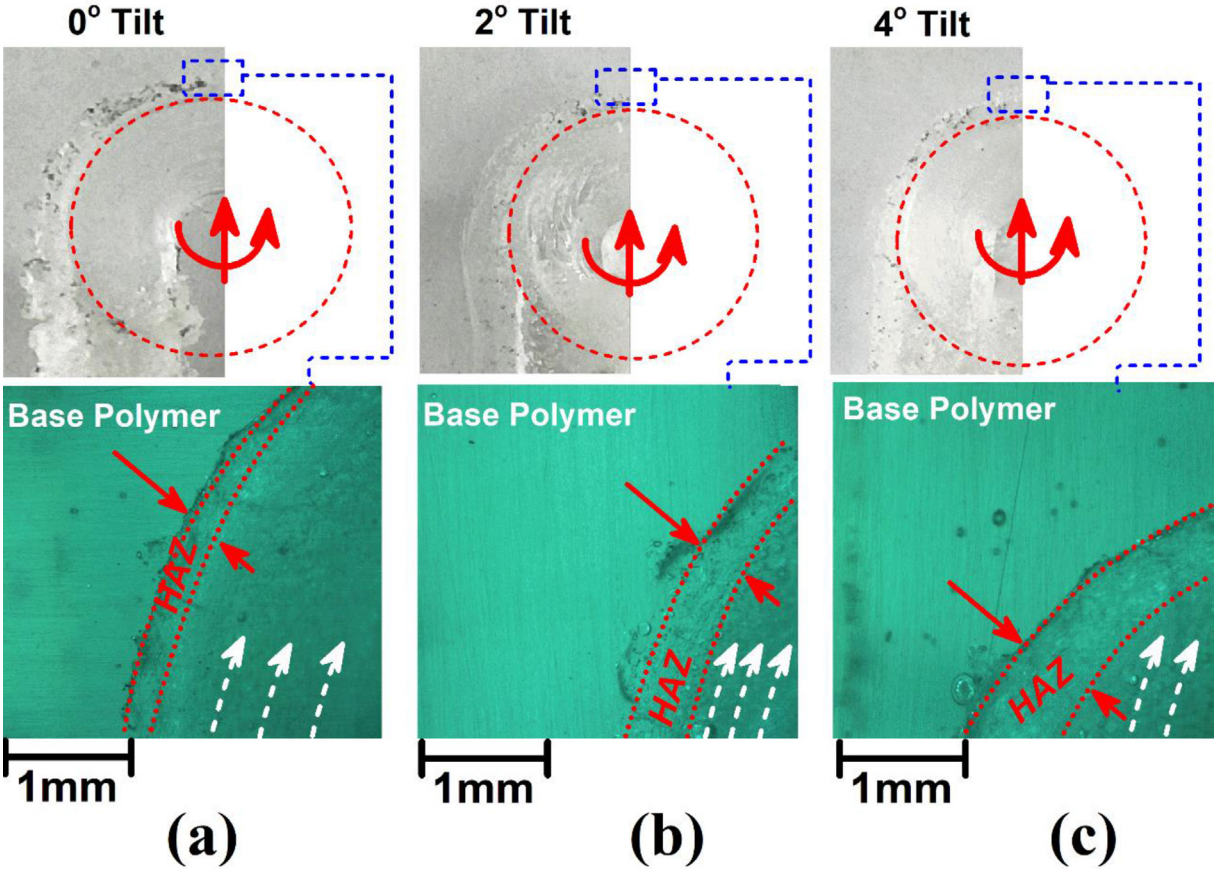

Fig. 10 – Experimental results of HAZ thickness at joint that FSJed with (a) 0°, (b) 2°, and (c) 4° TTA.

action of the tool can change it during the FSJ process. The simulation results of surface heat flux in joints with 0°, 2°, and 4° TTA are depicted in Fig. 9a, b, and 9c, respectively. The simulation results show that the heat flux has a deviation (γ) from the moving direction of the tool. The heat flux is concentrated in the backside of the tool and is due to the low heat transfer coefficient of PP. the results revealed that with increasing TTA, the deviation (γ) increases. It is known that the volume of PP in plasticized and molten forms is more than in a solid state of PP. During the FSJ, the PP heated up, and its volume increased, and after cooling down the joint line, the PP started to shrink [46].

During the tool's moving, the plasticized PP extruded from the retreating side (RS) to the advancing side (AS). Within this action, the concentration of PP in AS increases and leads to more heat concentration in AS. The high concentrate PP in AS pulls the material from RS, and this force bends the plasticized PP in AS. This phenomenon leads to the surface and joint line deviation (γ) heat flux. With increasing TTA, the γ increases due to higher heat generation in higher TTA. On the other hand, the simulation results revealed that narrow HAZ formed in the vicinity of the joint line (similar to the cross-section view), and with increasing heat input at high TTA, the thickness of HAZ on the surface of the joint line increases. The surface material flow of joints that FSJed with 0°, 2°, and 4° TTA are presented in Fig. 10a,b, and c, respectively. The main reason for this analysis is to determine how the TTA affects the HAZ area. The thickness of the HAZ area in lower TTA is formed thinner. Higher heat generation leads to more heat diffusion around the joint line and thicker HAZ formation. The HAZ thickness in 0°, 1°, 2°, 3°, and 4° TTA is measured at 0.2 mm, 0.3 mm, 0.4 mm, 0.55 mm, and 0.7 mm, respectively.

4.3. *Internal heat flux*

The simulation output from internal heat flux of 0°, 2°, and 4° TTA are depicted in Fig. 11a, b and c, respectively. The longitudinal section of heat flux was selected to analyze the results. As can be seen, the heat flux increases with increasing TTA. This phenomenon shows that increasing TTA, increases the preheating zone thickness in front of the tool. Consequently, the PP from the front into the stir zone extrudes easily. The surface flow of PP in joint lines welded at 0°, 2°, and 4° TTA are presented in Fig. 11d, e, and f, respectively.

Due to the properties of PP, the joint line cannot be appropriately formed at 0° TTA. The stirring action of the tool with 0° TTA seems unable to mix PP from the advancing side to the retreating side. For this reason, an incomplete stirring region is formed in 0° TTA, which is a significant defect in the joint line and makes an incomplete stir zone. On the other hand, the high TTA makes incomplete stirring and root-unfilling defects. At the higher TTA, two main issues happen

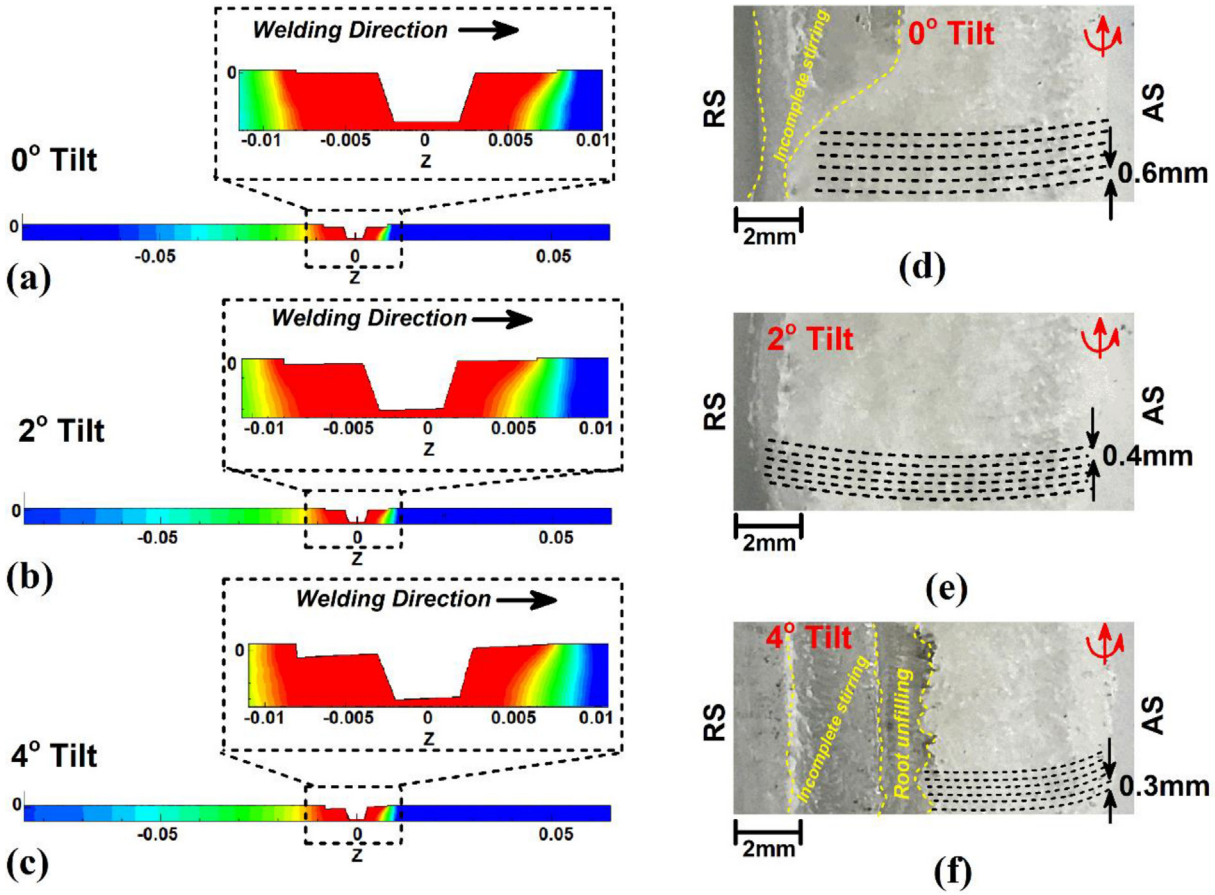

Fig. 11 – Longitudinal view of simulation results from joints that FSJed with (a) 0°, (b) 2°, and (c) 4° TTA. Surface flow of joints that FSJed with (d) 0°, (e) 2°, and (f) 4° TTA.

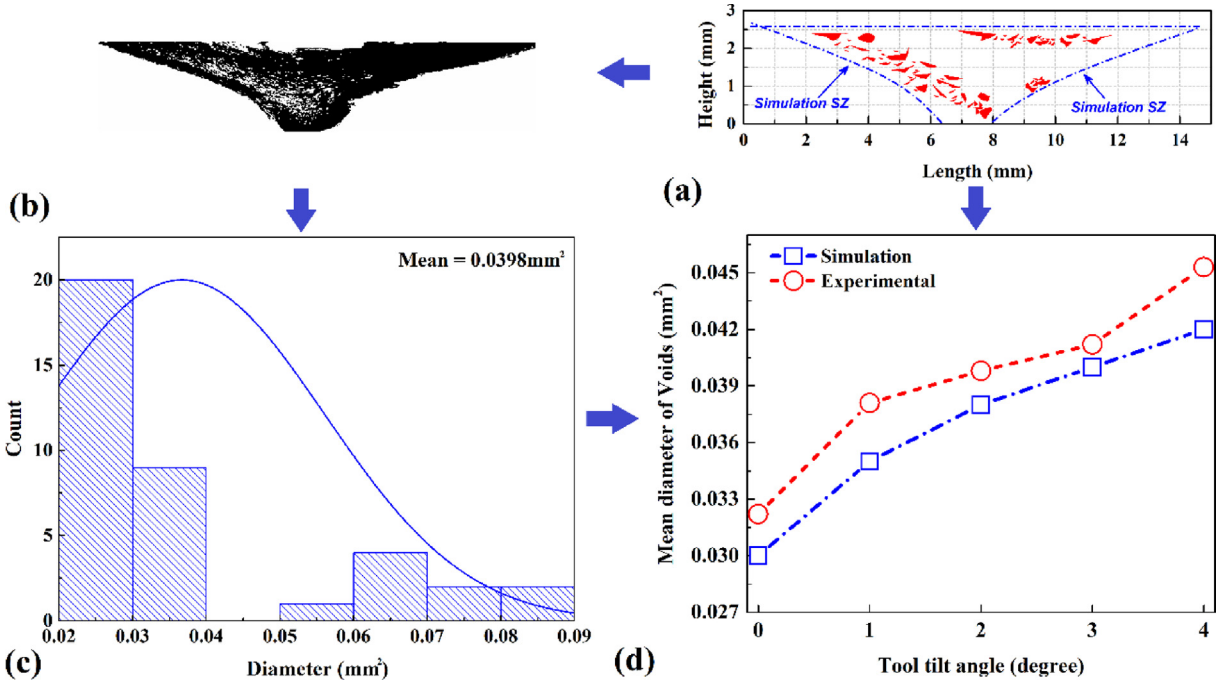

Fig. 12 – (a) Simulation result of internal defect formation in 2° TTA stir zone. (b) Image processing result of 2° TTA and (c) histogram of internal defects size in 2° TTA joint. (d) The comparison of internal defect formation between simulation results and experimental output.

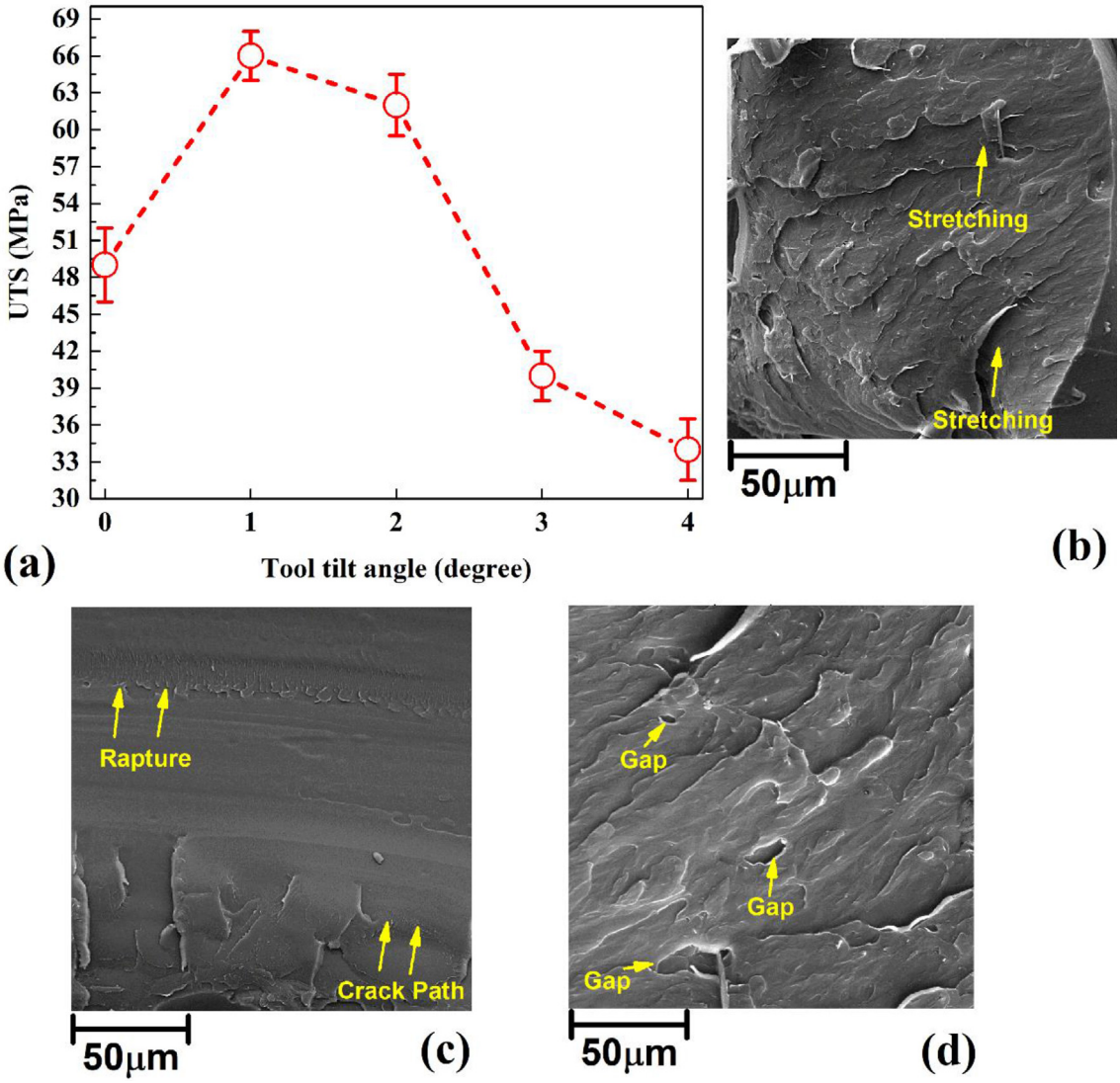

Fig. 13 – (a) UTS of final joint that produced by various TTA. SEM images of fracture surface of 1o TTA that shows (a) local stretching, (b) smooth fracture path and (d) internal microscale gaps on the fracture surface.

for the PP that leads to the formation of joint defects. At high TTA, the heat generation is high; in this case, the PP expands and runs out from the joint line. This effect leads to the material exit from the joint line, and the joint root cannot be filled, resulting in the incomplete stirring defect form. The mentioned effects are the main reason the FSJ joint line cannot be formed at high TTA.

The applied force at different TTA affects the PP compression behind the tool. The compression of PP in the joint line forms the flow rings at the surface. The results show that the distance of surface flow rings in joints welded within 0°, 1°, 2°, 3°, and 4° TTA is ~0.6 mm, ~0.5 mm, ~0.4 mm, ~0.4 mm, and ~0.3 mm, respectively. It shows that the joint line forms more compact at higher TTA, but the properties of PP prevent filling the joint line at higher TTA. Another defect that is formed during the FSJ of PP is internal gaps. The internal gaps are caused by trapping air bobbles during welding or losing the molecular weight of polymers after FSJ [42]. When PP lusts molecular weight during the FSJ process, the shrinkage properties of PP cause some micro hollow voids forms inside the joint line. During the simulation process, the boundary of PP sheets was without any reaction between surrounded air, and the simulation results predict the internal defect possibilities by shrinkage of PP after FSJ. An example of internal defects area by simulation in 2° TTA has depicted in Fig. 12a The red spots are shrinkage places in the stir zone. For better simulation output analysis, the FSJed sample's experimental results with 2° TTA are presented in Fig. 12b. The cross-section image is analysed by image processing software. The average diameter of internal gaps is measured and presented in Fig. 12c. This procedure is repeated for all samples, and a comparison between simulation outputs and experimental results is depicted in Fig. 12d. The simulation results have a difference from experimental data because the dropped air gap does not consider in simulation. The general trends show that the size of internal gaps increases at higher

TTA. The generated heat in the joint line plasticizes the PP, and after passing the FSJ tool, the plasticizes PP will be re-solid. This thermal cycle changes the PP properties and, due to obtained results, higher heat generation (at higher TTA) increases the size of internal defects. The minimum defects size was formed in 0° TTA (~0.033 mm^2), and maximum defects were formed in 4° TTA (~0.042 mm^2).

4.4. *Mechanical properties*

The mechanical properties of the final joint are related to the internal and external defects, the PP structure after welding, and the size of the stir zone. The tensile strength of FSJed samples was evaluated, and the ultimate tensile strength (UTS) of joints results are presented in Fig. 13a. The results show that the UTS of welded sample increased from 0° TTA to 1° TTA and after a slight decrease from 2° TTA dropped sharply. The low UTS of FSJed samples in 3° and 4° TTA is related to the incomplete joint line. The SZ of these samples was very small, with many defects, and for this reason, they were not able to tolerate tensile test stress. Consequently, the incomplete joint line decreases the UTS of PP after FSJ. The results indicated that the UTS of joints that FSJed with 0°, 1°, 2°, 3°, and 4° TTA were 48 MPa, 66 MPa, 62 MPa, 39 MPa, and 33 MPa, respectively.

The highest UTS achieved in the 1o TTA sample, and the lowest UTS recorded in 4° TTA. The SEM image from the fracture surface of 1° TTA joint (as the most robust sample) after the tensile test is presented in Fig. 13b, c, and d, respectively. The SEM results indicate a non-uniform fracture surface, which is expectable due to the complexity of the PP structure. The fracture of the PP sample was a brittle type, but in some areas, local stretching was detected (Fig. 13b). On the exterior sides of the tensile sample smooth crack path and final rapture were detected (Fig. 13c). This shows that the cracks initiation happened inside of the sample and growth path of crack was from inner sides of tensile sample into exterior sides. A close investigation of the fracture surface indicated gap holes. As discussed before, these gaps result from PP shrinkage and trapped air. Because the size of gaps in Fig. 13d is on a micro-scale, it would be concluded that these are the results of PP shrinkage. As can be seen, these gaps are the root of crack initiations.

5. Conclusion

The effects of TTA on heat generation, surface flow, internal flow, joint defects, and mechanical properties of FSJed PP were investigated. The FSJ of PP simulated by CFD technique and the simulation results compared with experimental outputs. The output of this study can be listed below.

1. The tool shoulder produces the maximum heat during the FSJ process, and the EA heat is generally produced by plastic deformation with tilted tool cases. The minimum heat was 192 °C, produced in 0° TTA, and the maximum heat was generated at 4° TTA sample 235 °C.
2. The high heat generation in TTA of more than 2° TTA decreases the dimension of the stir zone, PP exit from the joint line, and incomplete joint line. Joint lines with 1° TTA and 2° TTA formed defect free, and the biggest stir zone was formed with 17 mm^2 in 1° TTA.
3. The surface heat flux was not uniform due to the concentration of volumetric weight on the advancing side of the joint line. The high TTA leads to bigger HAZ and intense flow ring formation in the joint line, but material exit leads to root un-filling and incomplete stirring zone in the joint line at high TTA.
4. The internal gap made by shrinkage of PP and trapped air increased internal defect in the joint that FSJed at high TTA. These defects decreased the mechanical properties of the final joint. The most rebuts joint was produced in 1° TTA with 66 MPa ultimate tensile strength.

Declaration of Competing Interest

The authors declare that they have no known competing financial interests or personal relationships that could have appeared to influence the work reported in this paper.

REFERENCES

[1] Rehman RU, Sheikh-Ahmad J, Deveci S. Effect of preheating on joint quality in the friction stir welding of bimodal high density polyethylene. Int J Adv Manuf Technol 2021;117:455–68. https://doi.org/10.1007/s00170-021-07740-w.
[2] Aghajani Derazkola H, Simchi A. Processing and characterizations of polycarbonate/alumina nanocomposites by additive powder fed friction stir processing. Thin-Walled Struct 2020;157:107086. https://doi.org/10.1016/j.tws.2020.107086.
[3] Lambiase F, Derazkola HA, Simchi A. Friction stirwelding and friction spot stir welding processes of polymers-state of the art. Materials 2020;13.
[4] Lambiase F, Paoletti A, Durante M. Mechanism of bonding of AA7075 aluminum alloy and CFRP during friction assisted joining. Compos Struct 2021;261:113593. https://doi.org/10.1016/j.compstruct.2021.113593.
[5] Kosturek R, Slezak T, Torzewski J, Wachowski M, Sniezek L. Study on tensile and fatigue failure in the low-hardness zone of AA2519-T62 FSW joint. Manuf Rev 2022;9:25. https://doi.org/10.1051/mfreview/2022023.
[6] Kubit A, Wydrzynski D, Trzepiecinski T. Refill friction stir spot welding of 7075-T6 aluminium alloy single-lap joints with polymer sealant interlayer. Compos Struct 2018;201:389–97. https://doi.org/10.1016/j.compstruct.2018.06.070.
[7] Asmael M, Safaei B, Kalaf O, Zeeshan Q, Aldakheel F, Nasir T, et al. Recent developments in tensile properties of friction welding of carbon fiber-reinforced composite: a review. Nanotechnol Rev 2022;11:1408–36. https://doi.org/10.1515/ntrev-2022-0083.
[8] Kosturek R, Mierzyński J, Wachowski M, Torzewski J, Śnieżek L. The influence of tool traverse speed on the low cycle fatigue properties of AZ31 friction stir welded joints. Procedia Struct Integ 2022;36:153–8. https://doi.org/10.1016/j.prostr.2022.01.017.
[9] Guo Z, Ma T, Li W, Zhang Y, Zhao Z, Tao J, et al. Intergrowth bonding mechanism and mechanical property of linear

friction welded dissimilar near-alpha to near-beta titanium alloy joint. Adv Eng Mater 2021;23:2001479. https://doi.org/10.1002/adem.202001479.
[10] Guo Z, Ma T, Yang X, Chen X, Tao J, Li J, et al. Linear friction welding of Ti60 near-α titanium alloy: investigating phase transformations and dynamic recrystallization mechanisms. Mater Char 2022;194:112424. https://doi.org/10.1016/j.matchar.2022.112424.
[11] Mohan DG, Gopi S, Tomków J, Memon S. Assessment of corrosive behaviour and microstructure characterization of hybrid friction stir welded martensitic stainless steel. Adv Mater Sci 2021;21:67–78. https://doi.org/10.2478/adms-2021-0025.
[12] Hou W, Ahmad Shah LH, Huang G, Shen Y, Gerlich A. The role of tool offset on the microstructure and mechanical properties of Al/Cu friction stir welded joints. J Alloys Compd 2020;825:154045. https://doi.org/10.1016/j.jallcom.2020.154045.
[13] Choudhary M, Sharma A, Aravind Raj S, Sultan MTH, Hui D, Shah AUM. Contemporary review on carbon nanotube (CNT) composites and their impact on multifarious applications. Nanotechnol Rev 2022;11:2632–60. https://doi.org/10.1515/ntrev-2022-0146.
[14] Hou W, Ding Y, Huang G, Huda N, Shah LHA, Piao Z, et al. The role of pin eccentricity in friction stir welding of Al-Mg-Si alloy sheets: microstructural evolution and mechanical properties. Int J Adv Manuf Technol 2022;121:7661–75. https://doi.org/10.1007/s00170-022-09793-x.
[15] Wang S, Xu Y, Wang W, Tian Y, Zhang X, Huang H, et al. Enhancing interfacial bonding in friction stir lap welding of light metal and carbon fiber reinforced polymer composite. J Manuf Process 2022;83:729–41. https://doi.org/10.1016/j.jmapro.2022.09.038.
[16] Saeedy S, Besharati MK. Investigation of the effects of critical process parameters of friction stir welding of polyethyleneg. Proc Inst Mech Eng Part B J Eng Manuf 2011;225:1305–10. https://doi.org/10.1243/09544054JEM1989.
[17] Panneerselvam K, Lenin K. Investigation on effect of tool forces and joint defects during FSW of polypropylene plate. Procedia Eng 2012;38:3927–40. https://doi.org/10.1016/j.proeng.2012.06.450.
[18] Panneerselvam K, Lenin K. Joining of Nylon 6 plate by friction stir welding process using threaded pin profile. Mater Des 2014;53:302–7. https://doi.org/10.1016/j.matdes.2013.07.017.
[19] Azarsa E, Mostafapour A. Experimental investigation on flexural behavior of friction stir welded high density polyethylene sheets. J Manuf Process 2014;16:149–55. https://doi.org/10.1016/j.jmapro.2013.12.003.
[20] Dashatan SH, Azdast T, Ahmadi SR, Bagheri A. Friction stir spot welding of dissimilar polymethyl methacrylate and acrylonitrile butadiene styrene sheets. Mater Des 2013;45:135–41. https://doi.org/10.1016/j.matdes.2012.08.071.
[21] Simoes F, Rodrigues DM. Material flow and thermo-mechanical conditions during Friction Stir Welding of polymers: literature review, experimental results and empirical analysis. Mater Des 2014;59:344–51. https://doi.org/10.1016/j.matdes.2013.12.038.
[22] Vakili-Tahami F, Adibeig MR, Hassanifard S. Optimizing creep lifetime of friction stir welded PMMA pipes subjected to combined loadings using rheological model. Polym Test 2019;79:106049. https://doi.org/10.1016/j.polymertesting.2019.106049.
[23] Kunnathur Periyasamy Y, Perumal AV, Kunnathur Periyasamy B. Optimization of process parameters on friction stir welding of AA7075-T651 and AA6061 joint using response surface methodology. Mater Res Express 2019;6:96558. https://doi.org/10.1088/2053-1591/ab302e.
[24] Aghajani Derazkola H, Simchi A, Lambiase F. Friction stir welding of polycarbonate lap joints: relationship between processing parameters and mechanical properties. Polym Test 2019;79:105999. https://doi.org/10.1016/j.polymertesting.2019.105999.
[25] Aghajani Derazkola H, Simchi A. Experimental and thermomechanical analysis of friction stir welding of poly(methyl methacrylate) sheets. Sci Technol Weld Join 2018;23:209–18. https://doi.org/10.1080/13621718.2017.1364896.
[26] Eyvazian A, Hamouda AM, Aghajani Derazkola H, Elyasi M. Study on the effects of tool tile angle, offset and plunge depth on friction stir welding of poly(methyl methacrylate) T-joint. Proc Inst Mech Eng Part B J Eng Manuf 2020;234:773–87. https://doi.org/10.1177/0954405419889180.
[27] Zhai M, Wu CS, Su H. Influence of tool tilt angle on heat transfer and material flow in friction stir welding. J Manuf Process 2020;59:98–112. https://doi.org/10.1016/j.jmapro.2020.09.038.
[28] Zhai M, Wu CS, Shi L. Tool tilt angle induced variation of shoulder-workpiece contact condition in friction stir welding. Sci Technol Weld Join 2022;27:68–76. https://doi.org/10.1080/13621718.2021.2013709.
[29] Pereira MAR, Amaro AM, Reis PNB, Loureiro A. Effect of friction stir welding techniques and parameters on polymers joint efficiency—a critical review. Polymers 2021;13.
[30] Bilici MK. Effect of tool geometry on friction stir spot welding of polypropylene sheets. Express Polym Lett 2012;6:805–13. https://doi.org/10.3144/expresspolymlett.2012.86.
[31] Kiss Z, Czigany T. Microscopic analysis of the morphology of seams in friction stir welded polypropylene. Express Polym Lett 2012;6:54–62. https://doi.org/10.3144/expresspolymlett.2012.6.
[32] Moochani A, Omidvar H, Ghaffarian SR, Goushegir SM. Friction stir welding of thermoplastics with a new heat-assisted tool design: mechanical properties and microstructure. Weld World 2019;63:181–90. https://doi.org/10.1007/s40194-018-00677-x.
[33] Sahu SK, Mishra D, Mahto RP, Sharma VM, Pal SK, Pal K, et al. Friction stir welding of polypropylene sheet. Eng Sci Technol an Int J 2018;21:245–54. https://doi.org/10.1016/j.jestch.2018.03.002.
[34] Nath RK, Jha V, Maji P, Barma JD. A novel double-side welding approach for friction stir welding of polypropylene plate. Int J Adv Manuf Technol 2021;113:691–703. https://doi.org/10.1007/s00170-021-06602-9.
[35] Nath RK, Maji P, Barma JD. Development of a self-heated friction stir welding tool for welding of polypropylene sheets. J Brazilian Soc Mech Sci Eng 2019;41:553. https://doi.org/10.1007/s40430-019-2059-2.
[36] Zhai M, Wu C, Shi L. Numerical simulation of friction stir lap welding of Al-to-Mg alloys under different lap configurations and pin lengths. J Mater Res Technol 2022;20:2889–904. https://doi.org/10.1016/j.jmrt.2022.08.047.
[37] Elangovan K, Balasubramanian V, Valliappan M. Effect of tool pin profile and tool rotational speed on mechanical properties of friction stir welded AA6061 aluminium alloy. Mater Manuf Process 2008;23:251–60. https://doi.org/10.1080/10426910701860723.
[38] Ji H, Deng YL, Xu HY, Yin X, Zhang T, Wang WQ, et al. Numerical modeling for the mechanism of shoulder and pin features affecting thermal and material flow behavior in friction stir welding. J Mater Res Technol 2022;21:662–78. https://doi.org/10.1016/j.jmrt.2022.09.070.
[39] Zhang G, Wu C, Gao J. Ultrasonic line source and its coupling with the tool induced heat generation and material flow in friction stir welding. J Mater Res Technol 2022;21:502–18. https://doi.org/10.1016/j.jmrt.2022.09.053.

[40] Aghajani Derazkola H, Simchi A. Experimental and thermomechanical analysis of the effect of tool pin profile on the friction stir welding of poly(methyl methacrylate) sheets. J Manuf Process 2018;34:412–23. https://doi.org/10.1016/j.jmapro.2018.06.015.
[41] Aghajani Derazkola H, Kordani N, Aghajani Derazkola H. Effects of friction stir welding tool tilt angle on properties of Al-Mg-Si alloy T-joint. CIRP J Manuf Sci Technol 2021;33:264–76. https://doi.org/10.1016/j.cirpj.2021.03.015.
[42] Aghajani Derazkola H, Garcia E, Elyasi M. Underwater friction stir welding of PC: experimental study and thermo-mechanical modelling. J Manuf Process 2021;65:161–73. https://doi.org/10.1016/j.jmapro.2021.03.034.
[43] Iqbal MP, Jain R, Pal SK, Mandal P. Numerical modelling of friction stir welding of pipes: effect of tool shoulder on mechanical property and metallurgical characterization. J Manuf Process 2022;79:326–39. https://doi.org/10.1016/j.jmapro.2022.04.028.
[44] Chupradit S, Bokov DO, Suksatan W, Landowski M, Fydrych D, Abdullah ME, et al. Pin angle thermal effects on friction stir welding of AA5058 aluminum alloy: CFD simulation and experimental validation. Materials 2021;14:7565. https://doi.org/10.3390/ma14247565.
[45] Yang C, Dai Q, Shi Q, Wu C, Zhang H, Chen G. Flow-coupled thermo-mechanical analysis of frictional behaviors at the tool-workpiece interface during friction stir welding. J Manuf Process 2022;79:394–404. https://doi.org/10.1016/j.jmapro.2022.05.003.
[46] Khalaf HI, Al-Sabur R, Demiral M, Tomków J, Łabanowski J, Abdullah ME, et al. The effects of pin profile on HDPE thermomechanical phenomena during FSW. Polymers 2022;14:4632. https://doi.org/10.3390/polym14214632.